


 Cite this: *RSC Adv.*, 2020, 10, 17302

# Promoting formic acid oxidation performance of Pd nanoparticles *via* Pt and Ru atom mediated surface engineering†

 Dinesh Bhalothia,<sup>a</sup> Tzu-Hsi Huang,<sup>b</sup> Pai-Hung Chou,<sup>b</sup> Kuan-Wen Wang<sup>\*b</sup> and Tsan-Yao Chen<sup>\*ac</sup>

The alteration of surface functional properties *via* incorporation of foreign atoms is supposed to be a key strategy for the enhanced catalytic performance of noble-metal based nanocatalysts (NCs). In the present study, carbon-supported palladium (Pd)-based NCs including Pd, PdPt and PdRuPt have been prepared *via* a polyol reduction method under the same reduction conditions as for formic acid oxidation reaction (FAOR) applications. By cross-referencing the results of the microscopic, spectroscopic and electrochemical analysis we demonstrated that adding a small amount of platinum (Pt) into Pd NCs (*i.e.* PdPt NCs) significantly promotes the FAOR performance as compared to that of Pd NCs *via* weakening the CO<sup>ads</sup> bond strength at a lower voltage (0.875 V vs. NHE) than Pd (0.891 V vs. NHE). Of special relevance, the PdPt NC shows a mass activity (MA) of 1.0 A mg<sup>-1</sup> and 1.9 A mg<sup>-1</sup>, respectively, in the anodic and cathodic scan. These values are ~1.7-fold (0.6 A mg<sup>-1</sup>) and ~4.8-fold (0.4 A mg<sup>-1</sup>) higher than those of Pd NC. Moreover, PdPt NC retains a higher MA (54 mA mg<sup>-1</sup>) than that of Pd NC (9 mA mg<sup>-1</sup>) after chronoamperometric (CA) stability tests over 2000 s. Meanwhile, further addition of ruthenium (Ru) (*i.e.* PdRuPt NCs) outstandingly enhances the CO tolerance during the CA test *via* removal of adsorbed CO<sup>ads</sup> and thus shows the highest MA (62 mA mg<sup>-1</sup>) after CA testing, which is higher than that of PdPt (54 mA mg<sup>-1</sup>) and Pd (9 mA mg<sup>-1</sup>) NCs. The intriguing results obtained in this study have great significance to provide further strategic opportunities for tuning the surface electronic properties of Pd-based NCs to design Pd-based NCs with improved electrochemical performance.

 Received 11th February 2020  
 Accepted 18th April 2020

DOI: 10.1039/d0ra01303j

[rsc.li/rsc-advances](http://rsc.li/rsc-advances)

## Introduction

The ever-growing thrust of the global energy demand coupled with the confirmed near depletion of fossil fuels and their adverse climatic impacts have spurred the implementation of a carbon-neutral economy. In this context, direct formic acid fuel cells (DFAFCs) have garnered more appeal as potential clean energy-conversion systems owing to their high volumetric energy density and open circuit potential (1.45 V), lower fuel crossover effects and toxicity, enhanced energy conversion efficiency and robustness.<sup>1–4</sup> Despite these distinctive properties, the sluggish kinetics of the formic acid oxidation reaction (FAOR) at the anode counterpart severely restricts the development of commercially feasible DFAFCs.<sup>5,6</sup> Platinum (Pt)-based

nanocatalysts (NCs) are by far the best choice to boost FAOR kinetics.<sup>7</sup> However, limited reserves in the earth's crust and the high cost of Pt make them unfit for practical applications.<sup>8</sup> Moreover, Pt-based NCs are susceptible to poisoning (*i.e.* loss of surface active sites) by means of surface-adsorbed intermediates (such as CO) and thus exhibit poor durability in harsh redox conditions.<sup>9,10</sup> Consequently, development of FAOR NCs with an appropriate balance between catalytic performance (activity/stability) and noble-metal utilization is imperative. Aforementioned issues have been addressed by multidirectional efforts. More specifically, electronic properties of Pt-based NCs have been modified *via* introducing foreign atoms to generate multi-element nano-architectures including Pt–M alloys<sup>11–15</sup> (where M denotes foreign metals *e.g.* Pd, Pb, Ru, Sn, Ni *etc.*), M-core@Pt-shell nanostructures,<sup>16–19</sup> nanorods,<sup>20,21</sup> star-like nanocrystal,<sup>22</sup> nanowires,<sup>23,24</sup> nano-dendrites,<sup>25,26</sup> nano-frames,<sup>27,28</sup> nano-cages,<sup>29</sup> nano-sheets<sup>30</sup> or building a defect rich nano-structure (edges, corners, steps, low coordinate atoms).<sup>31</sup> In addition, recent studies have demonstrated that catalyst support is also a key player for determining the catalytic properties and significant improvements in performance have been shown by changing the catalyst support (*e.g.* carbon nanotubes (CNTs), reduced graphene oxide (rGO) *etc.*).<sup>32</sup> Moreover,

<sup>a</sup>Department of Engineering and System Science, National Tsing Hua University, Hsinchu 30013, Taiwan. E-mail: chencaeser@gmail.com; Tel: +886-3-5715131 ext. 34271

<sup>b</sup>Department of Materials and Mineral Resources Engineering, National Taipei University of Technology, Taipei 10608, Taiwan

<sup>c</sup>Hierarchical Green-Energy Materials (Hi-GEM) Research Centre, National Cheng Kung University, Tainan 70101, Taiwan

† Electronic supplementary information (ESI) available. See DOI: 10.1039/d0ra01303j



alternative catalyst design strategies by controlling the size,<sup>33</sup> shape,<sup>34</sup> and composition<sup>35</sup> of Pt-based NCs aimed at minimizing the Pt-content, while maintaining comparable performance are also at the forefront. Although, earlier pioneer endeavours laid the strong foundation for the development of efficient FAOR NCs, however, alternatives to Pt-based NCs are still in their infant stage.

In line with recent advancements, noble metals such as palladium (Pd) and ruthenium (Ru)-based nanomaterials are further applied for driving FAOR.<sup>36–40</sup> Among these, Pd retains a great part of the physicochemical properties similar to those of Pt and efficiently catalyze the FAOR. Even though Pd-lean NCs are potential contenders to substitute Pt for FAOR, nevertheless, a gap in catalytic performance comparative to Pt-based NCs still existed. To overcome this issue, hetero-catalytic systems are developed by alloying Pd with Pt or other transition metals (*e.g.* Co, Sn, Ni, Cu *etc.*) and proved to be effective for strengthening catalytic performance. In this event, the altered surface composition of NC leads to modified electronic properties and thus improves the catalytic performances.<sup>41,42</sup> Aforementioned arguments suggest that Pd is a possible alternative to catalyze FAOR, however, Pd is still a noble metal with limited reserves and is expensive, which prevents Pd-based NCs from “seizing the market”. Moreover, since the oxidation of formic acid involves the formation of CO intermediate, Ru can be added into catalysts to decrease the CO poisoning effect by modified reaction kinetics.<sup>43</sup>

To further unveil the better version of Pd-based FAOR NCs, in this study, we developed an efficient strategy to boost FAOR performance by changing the electronic properties of Pd nanoparticles *via* incorporating Pt and Ru atoms. The experimental samples (*i.e.* Pd, PdPt and PdRuPt) were prepared *via* polyol reduction method on the carbon support. By cross-referencing results of physical characterizations (high-resolution transmission electron microscopy (HRTEM), X-ray diffraction (XRD), X-ray photoelectron spectroscopy (XPS) and inductively coupled plasma-optical emission spectrometer (ICP-OES)) and electrochemical analysis (cyclic voltammogram (CV), linear sweep voltammogram (LSV), CO stripping and chronoamperometric (CA)), we demonstrated that addition of Pt atoms on Pd NPs greatly enhances the FAOR activity *via* lowering down the bond strength of intermediate adsorbents (*i.e.* CO<sub>ads</sub> bond strength). In this event, the onset potential of PdPt NC (875 mV) is significantly reduced as compared to that of Pd NPs (891 mV). Whereas, Ru has even better CO oxidation activity and thus adding Ru atoms to PdPt NC removes adsorbed CO<sub>ads</sub> and thus increase CO tolerance of PdRuPt NC.

## Experimental

### Preparation of experimental NCs

The experimental NCs were synthesized *via* the polyol reduction process. The Pd nanoparticles (NPs) were initially prepared by heating the mixture of palladium(II) chloride (PdCl<sub>2</sub>; Pd, 99%, Sigma-Aldrich Co.) (443 mg) and polyvinylpyrrolidone (PVP; MW = 10 000; 10 wt%) dissolved in 20 g of ethylene glycol (EG, Showa chemical Co. Ltd.) solvent at 160 °C for 2 h. After cooling

to room temperature, dark colloid was observed, indicating the formation of Pd NPs. In the second step, 0.25 g of as-prepared Pd NPs solution was added in a flask along with 12.5 g of 10 wt% PVP/EG solution, 9.95 g of EG and 88.66 mg of PdCl<sub>2</sub>. The resulting solution was mixed and kept at 160 °C for 2 h. In the next step, the obtained solution was cooled at room temperature and washed with acetone several times to remove the solvents. Subsequently, as-prepared Pd NPs were mixed with carbon black and added to an aqueous solution (10 mL) containing 1 mL of 0.5 M H<sub>2</sub>SO<sub>4</sub> and 1 mL of 1.0 M acetic acid. The solution was stirred vigorously at room temperature for 24 h. The resulting powder was washed with an adequate amount of acetone several times. Finally, the obtained precipitate was washed with sodium borohydride (NaBH<sub>4</sub>)/tert-butylamine (TBA) solution to remove PVP.

A similar method was adopted for the preparation of PdPt and PdRuPt NCs. For the preparation of PdPt NCs, 1295 mg H<sub>2</sub>PtCl<sub>6</sub>·6H<sub>2</sub>O (99%, Sigma-Aldrich Co.) was added in the first step to form Pt NPs. Whereas, PdRuPt NCs were synthesized by adding 0.25 g of as-prepared Pt NPs solution in a flask along with 12.5 g of 10 wt% PVP/EG solution, 9.95 g of EG, and 44.33 mg of PdCl<sub>2</sub>. The resulting solution was mixed and heated at 160 °C for 2 h. In a subsequent step, the obtained solution was cooled at room temperature and 51.8 mg of RuCl<sub>3</sub> was added. Afterwards, the solution was heated again at 160 °C for 2 h until all metal precursors were completely reduced. The resulting colloidal solution was cooled at room temperature and washed with acetone several times to remove the solvents. Finally, the as-prepared NPs and carbon black were added to the aqueous solution (10 mL) containing 1 mL of 0.5 M H<sub>2</sub>SO<sub>4</sub> and 1 mL of 1 M acetic acid. The solution was stirred vigorously at room temperature for 24 h. The resulting powders were precipitated and washed with acetone several times. Then the catalysts were washed with NaBH<sub>4</sub>/TBA solution to remove PVP and named as PdRuPt samples.

### Physical characterizations of experimental NCs

The physical properties of the experimental NCs were determined by cross-referencing results of microscopic and X-ray spectroscopic techniques. The average particle size and surface morphologies of the pristine NCs and post-chronoamperometric (CA) test were elucidated by using high-resolution transmission electron microscope (HRTEM) (JEOL JEM 2100F) equipped with a LaB<sub>6</sub> electron gun and operated at a maximum accelerating voltage of 200 kV. For the sample preparation, the NCs were ultrasonically suspended in isopropanol (IPA) and drop-casted on the 200 mesh copper grids. These specimens were then dried at 70 °C for 12 h in the oven. Before loading into the HRTEM chamber, the specimens were cleaned by plasma to remove the contaminated species on the surface of specimens. The crystal phases and structure of the NCs were determined by X-ray diffraction (XRD) analysis. The diffraction patterns of experimental NCs were measured in a 2θ range from 20° to 80° at a scan rate of 0.0124° s<sup>-1</sup> at a commercial diffractometer (Rigaku, Cu Kα (λ = 1.54 Å), operating at 40 kV and 40 mA). The X-ray photoelectron



spectroscopy (XPS) (Thermo VG Scientific Sigma Probe, operated at a voltage of 20 kV and a current of 30 mA) with a monochromatic X-ray source (Al K $\alpha$ ) was employed to investigate the oxidation states and surface compositions of the experimental NCs. The surface compositions of the catalysts were estimated by calculating the integral of each peak. Shirley type background was used to subtract the original peak, and then a combination of Lorentzian and Gaussian lines was applied to fit the experimental curve. Accurate binding energies were determined by reference to the C 1s peak at 284.6 eV. The atomic compositions of the experimental NCs were obtained *via* ICP-AES (Jarrell-Ash, ICAP 9000) analysis. The exact atomic ratios of Pd/Ru/Pt in Pd, PdPt, and PdRuPt NCs determined by ICP-AES is 100/0/0, 98/0/2, and 86/10/4, respectively.

### Preparation of the electrode and electrochemical measurements

Electrochemical measurements were performed at room temperature ( $25 \pm 1$  °C) using a potentiostat (CH Instruments Model 700A, CHI 700A) equipped with an electrochemical cell

consisting of the three-electrode system. Catalyst ink for the experiment was prepared by ultrasonically dispersing 5.0 mg of catalyst powder in 1.0 mL of isopropanol (IPA) and 50  $\mu$ L of Nafion (5 wt%, DuPont). To conduct the electrochemical test, 10.0  $\mu$ L of catalyst ink was drop-casted and air-dried on a glassy carbon rotating disk electrode (RDE) (0.196 cm $^2$  area) as the working electrode. A saturated calomel electrode (SCE) and a Pt wire were used as a reference electrode and counter electrode, respectively. All potentials in this study were referenced to the normal hydrogen electrode (NHE).

To identify the electrochemical performance of experimental NCs in FAOR, 0.5 M H $_2$ SO $_4$  + 0.5 M HCOOH aqueous solution was used as the electrolyte and was saturated with high-purified N $_2$  at room temperature. Prior to each electrochemical test, the electrodes were cycled several times between 0 and 1.4 V, to produce clean surfaces at a scan rate of 50 mV s $^{-1}$ . Formic acid oxidation current was measured by linear sweep voltammetry (LSV) with a scan rate of 20 mV s $^{-1}$  between 0 and 1.05 V. The mass activity (MA) was computed by using the following equations:

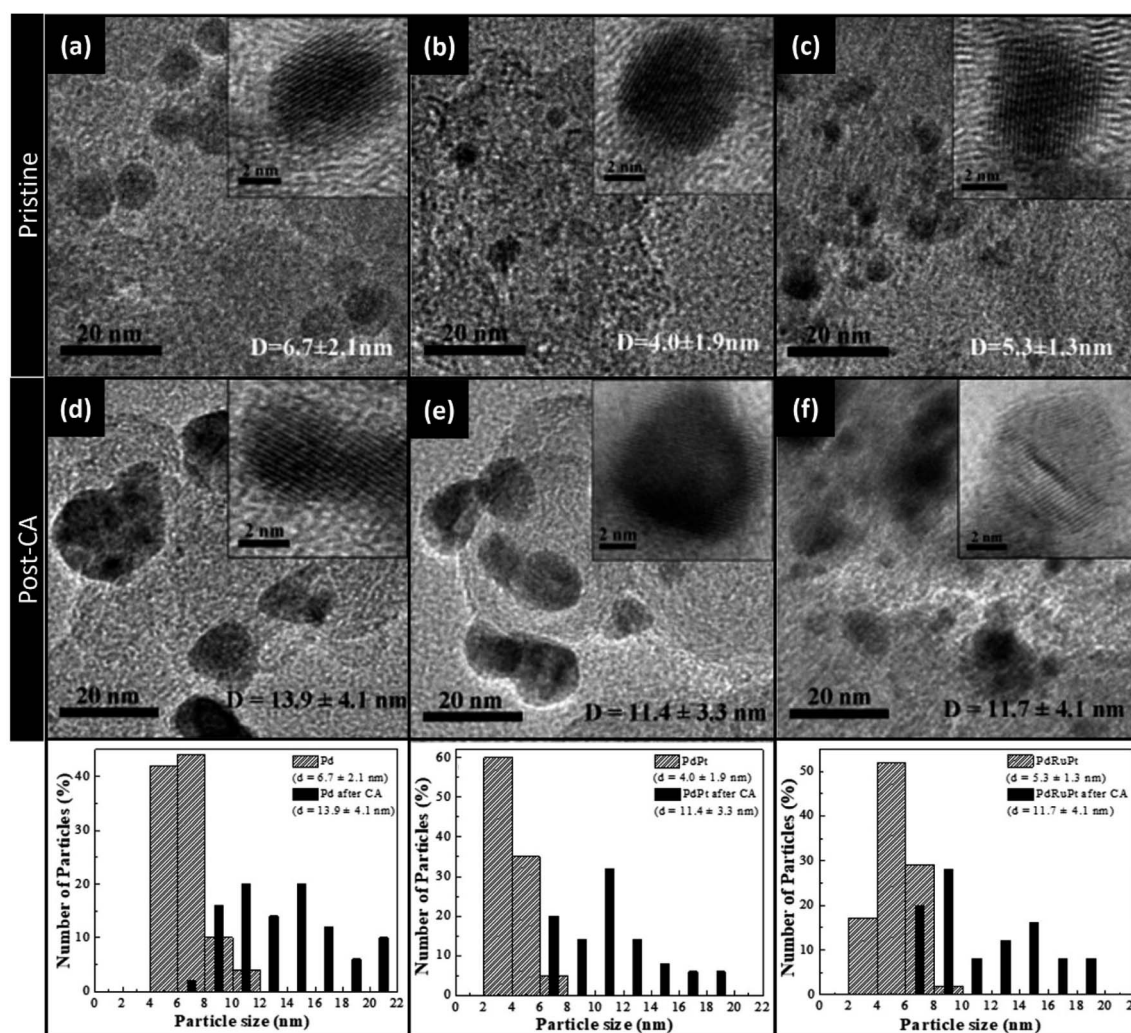


Fig. 1 HRTEM images of the pristine (a) Pd, (b) PdPt and (c) PdRuPt NCs, and (d) Pd, (e) PdPt and (f) PdRuPt NCs after chronoamperometric stability test. The particle-size distribution histograms of pristine and post chronoamperometric stability test are depicted in insets (bottom).



$$MA \text{ (Pt + Pd)} = \frac{I}{[\text{Pt}] + [\text{Pd}]} \quad (1)$$

where  $I$  represented the current density and  $[\text{Pt}] + [\text{Pd}]$  represented the Pt and Pd loading ( $\text{mg cm}^{-2}$ ) on the electrode, respectively. All current densities are normalized by the electrode area and metal loading on the electrode.

The cyclic voltammetry (CV) plots were recorded at a scan rate of  $20 \text{ mV s}^{-1}$  in  $\text{N}_2$ -saturated  $0.5 \text{ M H}_2\text{SO}_4$  aqueous solution between  $0.0$  and  $1.2 \text{ V}$ . The chronoamperometric (CA) test, which was performed to characterize the electrochemical stability and performance of the experimental NCs for FAOR, was conducted at the potential of  $0.5 \text{ V}$  for  $2000 \text{ s}$ . Moreover, for the CO stripping tests, the adsorption of CO on the NCs surface was performed by purging CO into  $0.5 \text{ M H}_2\text{SO}_4$  at  $0.34 \text{ V}$  for  $60 \text{ min}$ . Afterwards, the CO stripping voltammetry was measured between  $-0.1$  and  $1.20 \text{ V}$  in  $\text{N}_2$  saturated  $0.5 \text{ M H}_2\text{SO}_4$  solution at a scan rate of  $50 \text{ mV s}^{-1}$ .

## Results and discussion

### Surface morphology and crystal structure

HRTEM analysis revealed the crystal structure, shape and interplanar spacing of experimental NCs. Fig. 1 depicts HRTEM images and particle-size distribution histograms of the as-prepared NCs (pristine) and after CA analysis. It is evident from Fig. 1a–c that all NCs have been grown with a typical diameter of  $4\text{--}7 \text{ nm}$ . Whereas the average particle size of as-prepared Pd, PdPt, and PdRuPt NCs is about  $6.7 \pm 2.1$ ,  $4.0 \pm 1.9$ , and  $5.3 \pm 1.3 \text{ nm}$ , respectively. As observed, all experimental NCs show obvious aggregation after the durability test (Fig. 1d–f), suggesting the grain growth, migration, and dissolution of metals during CA test.

The lattice strain, average coherent length ( $D_{\text{avg}}$ ), and crystallinity of the as-prepared experimental NCs were determined by XRD analysis. Fig. 2 presents the XRD patterns of experimental NCs. The diffraction peak centred nearly at  $2\theta \sim 25^\circ$  is attributed to the XC-72R carbon support. Meanwhile, for PdPt NC, the three peaks centred nearly at  $\sim 39.8$ ,  $46.3$  and  $67.8^\circ$  are corresponding to diffraction signals from (111), (200) and (220) planes of metallic face-centred cubic (FCC) Pd. As compared to that of (111), (200) and (220) planes (JCPDS 87-0643) of face-centred cubic (FCC) Pd, the peaks of PdPt NC are shifted toward smaller angles (left side). The offset of diffraction peaks to lower angle reflects the lattice expansion (*i.e.* expansive strain) in PdPt NC. Such characteristics are obvious due to the addition of Pt NPs with a larger atomic size ( $1.39 \text{ \AA}$ ) than Pd ( $1.37 \text{ \AA}$ ) NPs in PdPt NC. Whereas, in the case of PdRuPt NC, the addition of Ru with smaller atomic size ( $1.34 \text{ \AA}$ ) than Pd and Pt NPs leads to the positive-shifts (higher angles) of the diffraction peaks reflecting compressive strain.

X-ray photoelectron spectroscopy (XPS) is employed for investigating the surface chemical composition and binding energies of experimental NCs. Fig. 3 depicts the fitted XPS spectra in the Pt 4f and Pd 3d region for the experimental NCs. In a Pt 4f spectrum (Fig. 3a), the broad peaks located nearly

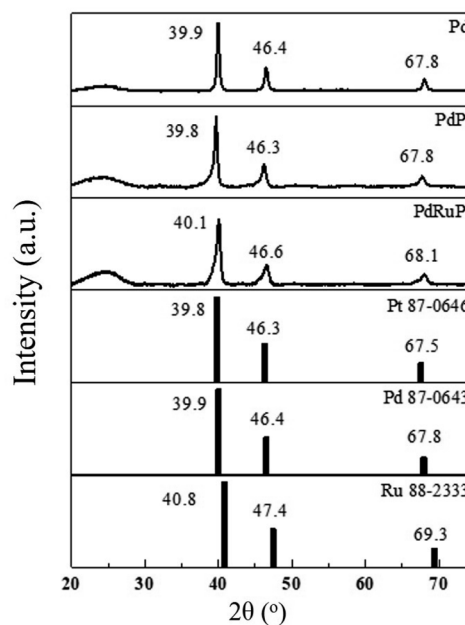


Fig. 2 XRD patterns of experimental NCs (Pd, PdPt and PdRuPt) and standard Pt, Pd and Ru samples.

about  $\sim 71 \text{ eV}$  and  $\sim 74 \text{ eV}$  are attributed to photoelectron emissions from Pt  $4f_{7/2}$  and Pt  $4f_{5/2}$  orbitals, respectively. Whereas for Pd 3d spectrum (Fig. 3b), the broad peaks centred nearly at  $\sim 336 \text{ eV}$  and  $\sim 341 \text{ eV}$  are responses for photoelectron emission from Pd  $3d_{5/2}$  and Pd  $3d_{3/2}$  orbitals, respectively. These emission peaks are further de-convoluted to reveal the extent of different oxidation states and corresponding results are given in Table 1. The binding energies of Pt  $4f_{7/2}$  peaks for PdPt and PdRuPt NCs are  $71$  and  $70.5 \text{ eV}$ , respectively. Such a significant change in binding energies ( $\Delta 0.5 \text{ eV}$ ) demonstrates that the Pt electronic structure of PdRuPt NC has been altered after incorporation of Ru-atoms, which is mainly attributed to the interaction between Pt and Pd and/or Ru components. Besides, these shifts in XPS binding energies can be rationalized by the difference in work function between pure Pt and the alloy, accompanied by re-hybridization of the d-band. Moreover, a negative shift ( $\Delta 0.5 \text{ eV}$ ) in the binding energy of Pt for PdRuPt NC ( $70.5 \text{ eV}$ ) as compared to that of PdPt NC ( $71 \text{ eV}$ ) results in downshifting of the d-band center. Further, such a reduced binding energy leads to a reduction of the adsorption energy of CO on PdRuPt NC surface.<sup>44</sup> On the other side, for Pd 3d orbital, the Pd/Pd<sup>2+</sup> ratio for Pd, PdPt, and PdRuPt NCs is  $71/29$ ,  $70/30$  and  $71/29$ , respectively. The Pd  $3d_{5/2}$  peak position for Pd, PdPt, and PdRuPt is  $335.9$ ,  $335.9$ , and  $335.5$ , respectively. Herein, the negative shift ( $\Delta 0.4 \text{ eV}$ ) for PdRuPt NC compared to PdPt NC may be attributed to the charge transfer from Ru to Pd atoms. The charge transfer to Pd induces downshift of the Pd d-band center which, in turn, induces weakening of Pd–adsorbate interaction on PdRuPt NC surface.<sup>45,46</sup> The weakening of adsorption between Pt, Pd atoms with inactive intermediates significantly influence the FAOR performance (consistently described in later section).<sup>47</sup>



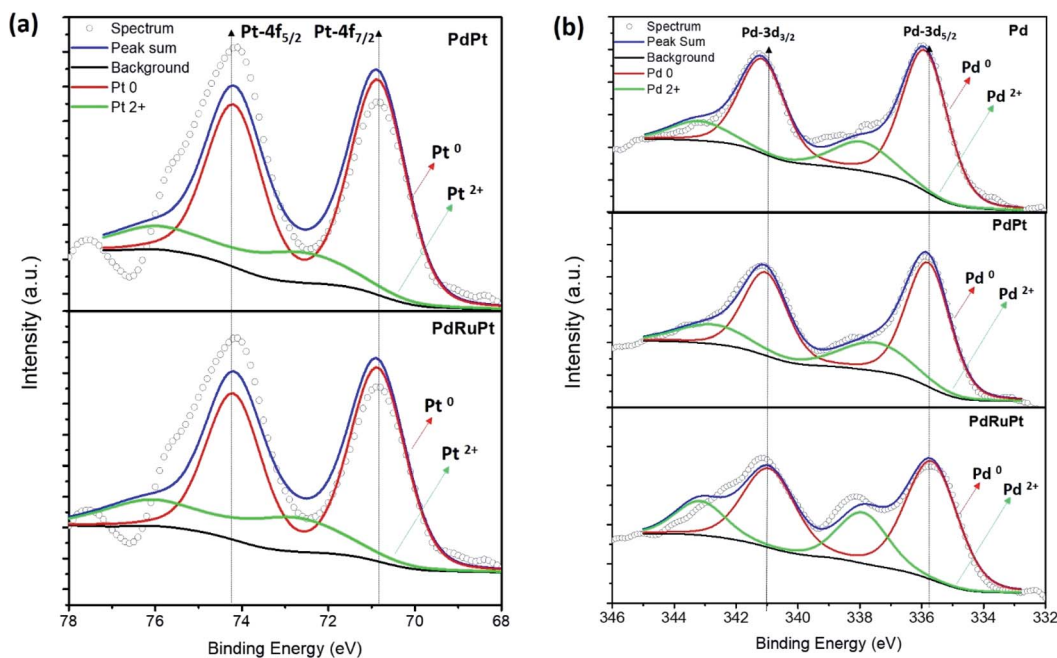


Fig. 3 X-ray photoelectron spectroscopy of experimental NCs. (a) Pt 4f of PdPt and PdRuPt NCs and (b) Pd 3d orbitals of Pd, PdPt and PdRuPt NCs.

Table 1 XPS determined composition ratios and binding energy of experimental NCs

Samples	Elemental chemical states				Surface composition (%)		Binding energies (eV)	
	Pt <sup>0</sup>	Pt <sup>2+</sup>	Pd <sup>0</sup>	Pd <sup>2+</sup>	Pt	Pd	Pt <sup>0</sup>	Pd <sup>0</sup>
PdRuPt	80	20	71	29	10	90	70.5	335.5
PdPt	76	24	70	30	9	91	71	335.9
Pd	NA	NA	71	29	NA	100	NA	335.9

To get further insight into the surface composition and to demonstrate the CO oxidation activity of as-prepared NCs with respect to surface species, CO-stripping analysis has been done. As exhibited in Fig. 4, the onset potentials for Pd, PdPt, and PdRuPt NCs is 891, 875, and 510 mV, respectively. Since surface Pt atoms can weaken the adsorbed CO bond at a lower voltage than Pd, the decrease in onset potential for PdPt compared to that for Pd suggests the surface Pt coverage.<sup>48</sup> Furthermore, for PdRuPt, Ru has even better CO oxidation activity than Pt, and the large negative-shifts in onset potential, when compared with Pd and PdPt, can be observed, suggesting the numerous surface Ru coverage on the ternary catalysis.<sup>49</sup>

Cyclic voltammogram (CV) of experimental NCs are presented in Fig. 5a. Accordingly, it can be observed that the CV curves exhibit three distinctive regions: hydrogen adsorption-desorption (*i.e.* under-potential deposition of hydrogen (UPD<sub>H</sub>)) below 300 mV, the double-layer region between 300 and 600 mV, and surface oxidation (forward scan)/surface oxides reduction (backward scan) at potentials above 600 mV. The changes in CV shape, related to changes in surface compositions, can be clearly observed for both regions. As

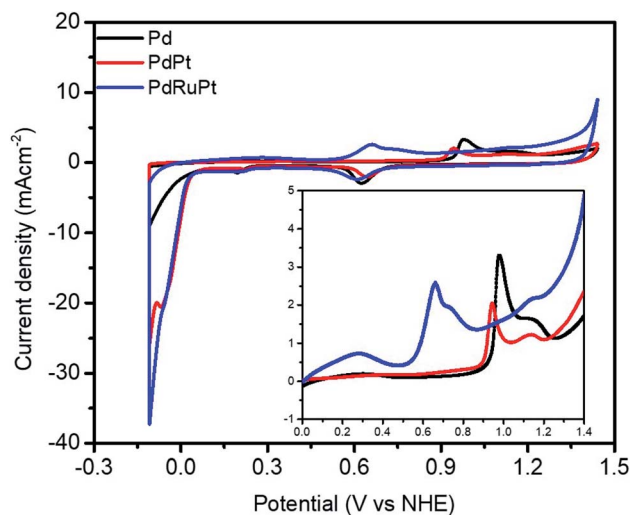


Fig. 4 The CO-stripping voltammogram of Pd, PdPt, and PdRuPt NCs.



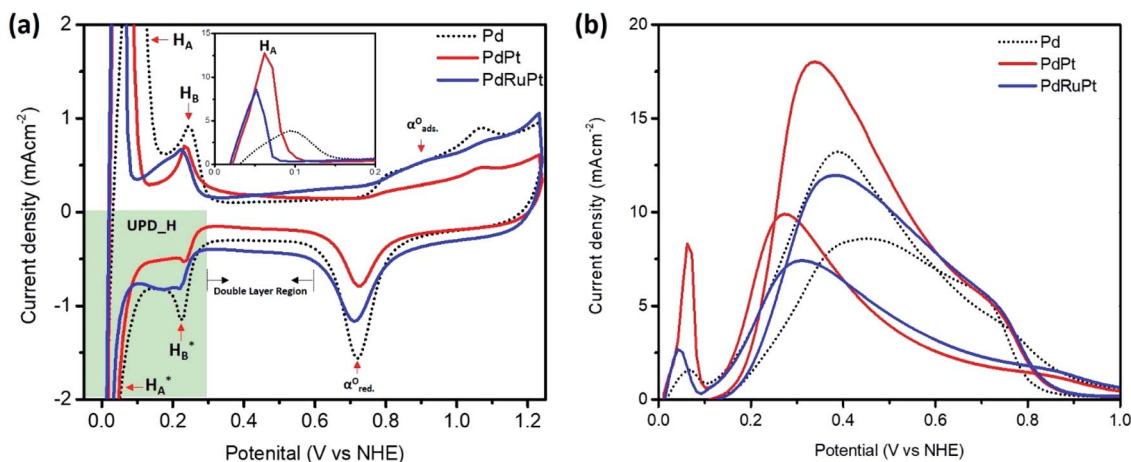


Fig. 5 (a) The CV curves of experimental NCs recorded in  $N_2$  saturated 0.5 M  $H_2SO_4$  electrolyte solution and (b) the LSV patterns of Pd, PdPt, and PdRuPt NCs recorded in  $N_2$  saturated 0.5 M  $H_2SO_4$  and 0.5 M  $HCOOH$  electrolyte solution.

shown in the inset of Fig. 5a, in the UPD\_H region, the hydrogen reductive absorption and oxidative desorption peaks ( $H_A$  in forward scan and  $H_A^*$  in backward scan) of PdPt, PdRuPt become sharper and higher than those of Pd. Moreover, the H species in and out of the PtPd and PdRuPt lattice interstices accompanied by  $H^+$  electro-reduction and H electro-oxidation on their surfaces in the negative and positive scans, respectively, resulting in the hydrogen absorption and desorption peaks shifted to relatively negative potentials. In the backward scan, the cathodic peak potential for reducing oxides on PdPt and PdRuPt tends to shift higher potentials when compared to Pd. Moreover, when compared with PdPt, the lower peak current in the hydrogen region of PdRuPt is due to the formation of Ru oxides at those potentials and larger currents in the double layer are attributed to oxide formation.<sup>50</sup>

Fig. 5b shows the linear sweep voltammetry (LSV) curves of experimental NCs measured in 0.5 M  $H_2SO_4$  and 0.5 M  $HCOOH$  electrolyte solution. In the LSV curves (Fig. 5b), all the experimental NCs exhibit peaks with suppressed intensity nearly at 0.05 V vs. NHE. These peaks are attributed to the direct oxidation of formic acid to  $CO_2$  by the dehydrogenation reaction. Whereas, intense anodic peaks centered nearly at  $\sim 0.3$ – $0.5$  V vs. NHE are corresponding to the indirect oxidation pathway for formic acid through an adsorbed CO intermediate.<sup>51</sup> For each NC, the onset potential measured from CO-stripping, the maximum current density in the forward and backward scan for FAOR, and the mass activity (MA) obtained when FAOR current

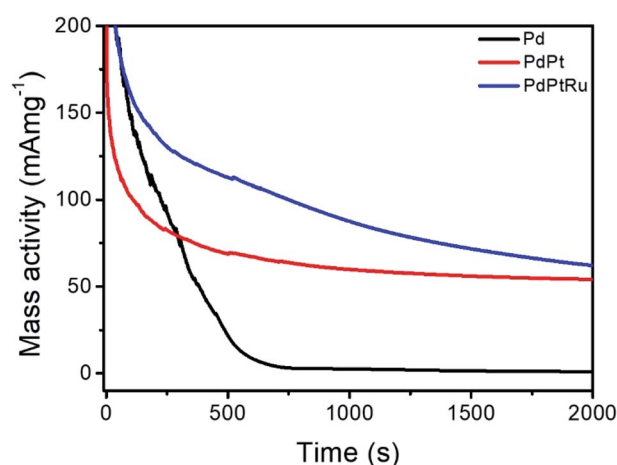


Fig. 6 The mass activity of experimental NCs after CA test over 2000 s.

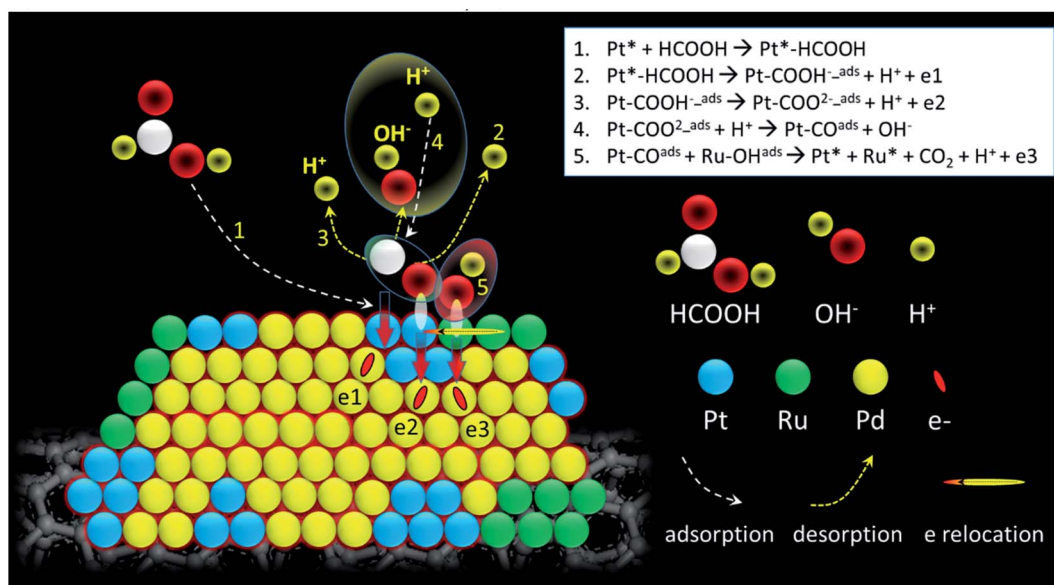
density was normalized to the Pt + Pd loading, are displayed in Table 2. The MA in the anodic/cathodic scan of Pd, PdPt, and PdRuPt, is 0.6/0.4, 1.0/1.9, and 0.9/1.4  $A\ mg^{-1}$ , respectively. It can be observed that the current density in the anodic scan is higher than that in the cathodic scan for Pd, showing that Pt atoms would strongly adsorb  $CO_{ads}$  at relatively low potentials, and quickly blocks the surface sites, but for Pd, the poisoning by  $CO_{ads}$  at low potentials is much slower. Besides, the interaction between Pd and low amounts of Pt, known as the third body

Table 2 Electrochemical results of Pd, PdPt, and PdRuPt

Samples	$E_{onset}^a$	$I_f$ ( $mA\ cm^{-2}$ )	$I_b$ ( $mA\ cm^{-2}$ )	$MA_f$ (Pt & Pd) ( $A\ mg^{-1}$ )	$MA_b$ (Pt & Pd) ( $A\ mg^{-1}$ )	$MA_f$ 05-2000 s ( $mA\ mg^{-1}$ )	ECSA ( $m^2\ g^{-1}$ )	$SA_f$ ( $mA\ cm^{-2}$ )	$SA_b$ ( $mA\ cm^{-2}$ )
Pd	0.891	12.6	8.2	0.6	0.4	9	187	0.70	0.46
PdPt	0.875	9.9	18.0	1.0	1.9	54	285	0.36	0.66
PdRuPt	0.510	7	11.2	0.9	1.4	62	204	0.40	0.64

<sup>a</sup> Calculated from CO stripping analysis.





**Scheme 1** Reaction coordinates of formic acid oxidation on PdRuPt surface. The first four steps adopt to all experimental samples. The 5th step, which is the key reaction step, only adopt in the presence of Ru atoms on catalyst surface.

effect can have a promoting effect on catalytic current, suggesting the higher total activity of PdPt than Pd.<sup>52</sup> For PdRuPt, the decrease of current density may be due to inactive surface Ru coverage, but the dissociation of water and the formation of OH species on Ru can remove the poisoning intermediates adsorbed on the active sites, known as the bi-functional mechanism, may enhance CO tolerance, and lead to higher anodic/cathodic current density ratio for PdRuPt than PdPt.<sup>53,54</sup> Also, downshift of the Pd d-band center which can weaken Pd-adsorbate interaction suggested by the XPS spectra may also result in the high MA<sub>f</sub>/MA<sub>b</sub> ratio.

The chrono-amperometric (CA) test has been applied to measure the stability of experimental NCs (Fig. 6). The results of MA after 2000 seconds stability test of NCs are listed in Table 2. PdPt shows higher MA than Pd because low amounts of Pt adding into Pd enhance the catalytic activity, change Pt electronic structure, and reduce the adsorption energy of CO. PdRuPt shows the highest MA after CA test may be due to existence of surface Ru, which can remove adsorbed CO<sub>ads</sub> and increase CO tolerance of catalysts.

Further evidence regarding changes in surface composition during CA stability test is obtained by measuring CV curves of post-CA samples (Fig. S1†). For Pd, the severe decrease of peak intensity in the hydrogen region may be due to agglomeration of NPs. During the stability test of PdPt, the cathodic peak potential does not shift significantly, suggesting that surface composition may not be obviously changed, and the decrease of peak intensity in the hydrogen region may be also due to agglomeration of NPs. For PdRuPt, the intensities of the hydrogen reductive absorption and oxidative desorption peaks become even higher after CA, suggesting that Pt surface segregation and metal dissolution may result in the increase of ECSA and further promoting their FAO. Combining results of electrochemical analyses (CO stripping, CV, and CA) and physical

structure inspections, the optimum durability of ternary nanocatalysts among experimental samples can be rationalized by the bifunctional mechanism in collaboration between Pd, Pt, and Ru atoms in its surface. From CV analysis, one can notice that the Ru atoms are mostly segregate in the PdRuPt surface. Such a characteristic is revealed by the smeared H<sub>2</sub> current peaks in UPD<sub>H</sub> region and the prevailing OH ligands (*i.e.*, high current density in the double-layer region (0.3 to 0.6 V vs. RHE)). Meanwhile, the surface composition is dominated by Pd atoms as depicted by the strong current peak for oxygen desorption in the backward sweep from 0.9 to 0.6 V vs. RHE. From XPS results (Table 1), Pt atoms are distributed in PdRuPt surface. In this event, compared to that of PdPt, reduced binding energy by 0.5 eV indicates a strong electron relocation to Pt atoms from the neighboring atoms. Such a strong electron relocation suppresses the binding energy of CO molecules in Pt and thus substantially reduces the onset potential of CO stripping peak by 0.33 V as compared to that of Pd nanocatalyst (Fig. 4). Therefore, the activity and durability of PdRuPt on FAO are facilitated by introducing high contents of OH in its surface (Scheme 1).

## Conclusion

In this study, Pd-based binary and ternary NCs including PdPt and PdRuPt have been synthesized *via* polyol reduction method and their FAOR performance has been investigated with respect to their surface compositions. As compared to Pd, the addition of Pt has shown great promotion of FAOR performance, which can be ascribed by means of weakening the CO<sup>ads</sup> bond strength. In this event, MA of PdPt NC is increased ~1.7-fold (1.0 A mg<sup>-1</sup>) and ~4.8-fold (1.9 A mg<sup>-1</sup>) in the anodic and cathodic scan, respectively, as compared to that of Pd NC. Moreover, PdPt NC shows higher MA (54 mA mg<sup>-1</sup>) as



compared to that of Pd NC ( $9 \text{ mA mg}^{-1}$ ) after the CA test over 2000 s, indicating the low amounts of Pt adding into Pd can enhance the catalytic activity. Meanwhile, PdRuPt NC shows highest CO tolerance during CA test (MA of PdRuPt NC after CA test is  $62 \text{ mA mg}^{-1}$ ) due to the existence of surface Ru, which can remove adsorbed  $\text{CO}^{\text{ads}}$  and increase CO tolerance of catalysts.

## Conflicts of interest

There are no conflicts to declare.

## Acknowledgements

This work was supported by Ministry of Science and Technology in Taiwan, R. O. C. (MOST 107-2628-E-008-003-MY3, MOST 108-3116-F-008-008, MOST 108-3116-F-007-001, and 109-3116-F-007-001). T.-Y. Chen acknowledges the financially supported by the Hierarchical Green-Energy Materials (Hi-GEM) Research Center of Ministry of Science and Technology in Taiwan, R. O. C. (MOST 107-3017-F-006-003).

## Notes and references

- 1 J. Kim, C.-W. Roh, S. K. Sahoo, S. Yang, J. Bae, J. W. Han and H. Lee, *Adv. Energy Mater.*, 2018, **8**, 1701476.
- 2 V. Mazumder and S. Sun, *J. Am. Chem. Soc.*, 2009, **131**, 4588–4589.
- 3 S. Ha, Z. Dunbar and R. I. Masel, *J. Power Sources*, 2006, **158**, 129–136.
- 4 X. Yu and P. G. Pickup, *J. Power Sources*, 2008, **182**, 124–132.
- 5 J. N. Tiwari, R. N. Tiwari, G. Singh and K. S. Kim, *Nano Energy*, 2013, **2**, 553–578.
- 6 B.-W. Zhang, H.-L. Yang, Y.-X. Wang, S.-X. Dou and H.-K. Liu, *Adv. Energy Mater.*, 2018, **8**, 1703597.
- 7 X. Han, X. Wu, Y. Deng, J. Liu, J. Lu, C. Zhong and W. Hu, *Adv. Energy Mater.*, 2018, **8**, 1870110.
- 8 E. Zagoraoui, M. K. Daletou, L. Sygellou, S. Ballomenou and S. G. Neophytides, *Appl. Catal., B*, 2019, **259**, 118050.
- 9 C. Rice, S. Ha, R. I. Masel and A. Wieckowski, *J. Power Sources*, 2003, **115**, 229–235.
- 10 J. Jiang and A. Kucernak, *J. Electroanal. Chem.*, 2002, **520**, 64–70.
- 11 S. Luo, W. Chen, Y. Cheng, X. Song, Q. Wu, L. Li, X. Wu, T. Wu, M. Li, Q. Yang, K. Deng and Z. Quan, *Adv. Mater.*, 2019, **31**, 1903683.
- 12 X. Jiang, Y. Liu, J. Wang, Y. Wang, Y. Xiong, Q. Liu, N. Li, J. Zhou, G. Fu, D. Sun and Y. Tang, *Nano Res.*, 2019, **12**, 323–329.
- 13 M. N. Krstajić Pajić, S. I. Stevanović, V. V. Radmilović, A. Gavrilović-Wohlmuther, P. Zabinski, N. R. Elezović, V. R. Radmilović, S. L. Gojković and V. M. Jovanović, *Appl. Catal., B*, 2019, **243**, 585–593.
- 14 M. S. Çögenli and A. B. Yurtcan, *Int. J. Hydrogen Energy*, 2018, **43**, 10698–10709.
- 15 Y. M. Asal, I. M. Al-Akraa, A. M. Mohammad and M. S. El-Deab, *Int. J. Hydrogen Energy*, 2019, **44**, 3615–3624.
- 16 A. Romero Hernández, E. M. Arce Estrada, A. Ezeta and M. E. Manríquez, *Electrochim. Acta*, 2019, **327**, 134977.
- 17 J. Zou, M. Wu, S. Ning, L. Huang, X. Kang and S. Chen, *ACS Sustainable Chem. Eng.*, 2019, **7**, 9007–9016.
- 18 N. Zhang, S. Guo, X. Zhu, J. Guo and X. Huang, *Chem. Mater.*, 2016, **28**, 4447–4452.
- 19 H. Xu, B. Yan, S. Li, J. Wang, C. Wang, J. Guo and Y. Du, *Chem. Eng. J.*, 2018, **334**, 2638–2646.
- 20 F. Gao, Y. Zhang, T. Song, C. Wang, C. Chen, J. Wang, J. Guo and Y. Du, *J. Colloid Interface Sci.*, 2020, **561**, 512–518.
- 21 T.-H. Huang, H.-S. Zheng, Y.-M. Cheng, C.-W. Liu, S.-W. Lee, J.-H. Wang and K.-W. Wang, *Sustainable Energy Fuels*, 2019, **3**, 3352–3362.
- 22 Y. Peng, L. Li, R. Tao, L. Tan, M. Qiu and L. Guo, *Nano Res.*, 2018, **11**, 3222–3232.
- 23 X. Jiang, G. Fu, X. Wu, Y. Liu, M. Zhang, D. Sun, L. Xu and Y. Tang, *Nano Res.*, 2018, **11**, 499–510.
- 24 J. Pei, J. Mao, X. Liang, Z. Zhuang, C. Chen, Q. Peng, D. Wang and Y. Li, *ACS Sustainable Chem. Eng.*, 2018, **6**, 77–81.
- 25 H. Xu, B. Yan, S. Li, J. Wang, C. Wang, J. Guo and Y. Du, *ACS Sustainable Chem. Eng.*, 2018, **6**, 609–617.
- 26 C. Zhai, H. Zhang, J. Hu, L. Zeng, M. Xue, Y. Du and M. Zhu, *J. Alloys Compd.*, 2019, **774**, 274–281.
- 27 W. Ye, S. Chen, M. Ye, C. Ren, J. Ma, R. Long, C. Wang, J. Yang, L. Song and Y. Xiong, *Nano Energy*, 2017, **39**, 532–538.
- 28 F. Saleem, B. Ni, Y. Yong, L. Gu and X. Wang, *Small*, 2016, **12**, 5261–5268.
- 29 H. Wang, Y. Li, K. Deng, C. Li, H. Xue, Z. Wang, X. Li, Y. Xu and L. Wang, *ACS Appl. Mater. Interfaces*, 2019, **11**, 4252–4257.
- 30 Q. Yang, L. Shi, B. Yu, J. Xu, C. Wei, Y. Wang and H. Chen, *J. Mater. Chem. A*, 2019, **7**, 18846–18851.
- 31 Y. Chen, H.-J. Niu, Y.-G. Feng, J.-H. Wu, A.-J. Wang, H. Huang and J.-J. Feng, *Appl. Surf. Sci.*, 2020, 145480, DOI: 10.1016/j.apsusc.2020.145480.
- 32 X. Ning, X. Zhou, J. Luo, L. Ma, X. Xu and L. Zhan, *Electrochim. Acta*, 2019, **319**, 129–137.
- 33 W. Zhou and J. Y. Lee, *J. Phys. Chem. C*, 2008, **112**, 3789–3793.
- 34 S. Akbar, A. Anwar, M. Z. Noon, J. M. Elliott and A. M. Squires, *Mater. Sci. Technol.*, 2019, **35**, 1–11.
- 35 Y. Xie and N. Dimitrov, *Appl. Catal., B*, 2020, **263**, 118366.
- 36 S. Hu, F. Munoz, J. Noborikawa, J. Haan, L. Scudiero and S. Ha, *Appl. Catal., B*, 2016, **180**, 758–765.
- 37 X. Yu and P. G. Pickup, *J. Power Sources*, 2008, **182**, 124–132.
- 38 H. Huang and X. Wang, *J. Mater. Chem.*, 2012, **22**, 22533–22541.
- 39 B. Jiang, H. Ataee-Esfahani, C. Li, S. M. Alshehri, T. Ahamad, J. Henzie and Y. Yamauchi, *Chem.–Eur. J.*, 2016, **22**, 7174–7178.
- 40 S. St. John, R. W. Atkinson, K. A. Unocic, R. R. Unocic, T. A. Zawodzinski and A. B. Papandrew, *ACS Catal.*, 2015, **5**, 7015–7023.
- 41 C. Wang, B. Peng, H.-N. Xie, H.-X. Zhang, F.-F. Shi and W.-B. Cai, *J. Phys. Chem. C*, 2009, **113**, 13841–13846.
- 42 H.-X. Zhang, C. Wang, J.-Y. Wang, J.-J. Zhai and W.-B. Cai, *J. Phys. Chem. C*, 2010, **114**, 6446–6451.





- 43 H. Gao, S. Liao, J. Zeng, Y. Xie and D. Dang, *Electrochim. Acta*, 2011, **56**, 2024–2030.
- 44 M. Wakisaka, S. Mitsui, Y. Hirose, K. Kawashima, H. Uchida and M. Watanabe, *J. Phys. Chem. B*, 2006, **110**, 23489–23496.
- 45 M. A. Matin, J.-H. Jang and Y.-U. Kwon, *J. Power Sources*, 2014, **262**, 356–363.
- 46 Z. Zhang, J. Ge, L. Ma, J. Liao, T. Lu and W. Xing, *Fuel Cells*, 2009, **9**, 114–120.
- 47 X. Yu and P. G. Pickup, *Electrochem. Commun.*, 2009, **11**, 2012–2014.
- 48 P. K. Babu, H. S. Kim, J. H. Chung, E. Oldfield and A. Wieckowski, *J. Phys. Chem. B*, 2004, **108**, 20228–20232.
- 49 A. C. Garcia, V. A. Paganin and E. A. Ticianelli, *Electrochim. Acta*, 2008, **53**, 4309–4315.
- 50 F. Colmati Jr., W. H. Lizcano-Valbuena, G. A. Camara, E. A. Ticianelli and E. R. Gonzalez, *J. Braz. Chem. Soc.*, 2002, **13**, 474–482.
- 51 A. K. Taylor, D. S. Perez, X. Zhang, B. K. Pilapil, M. H. Engelhard, B. D. Gates and D. A. Rider, *J. Mater. Chem. A*, 2017, **5**, 21514–21527.
- 52 B. Gralec and A. Lewera, *Appl. Catal., B*, 2016, **192**, 304–310.
- 53 W. Chen, L.-P. Xu and S. Chen, *J. Electroanal. Chem.*, 2009, **631**, 36–42.
- 54 T. Frelink, W. Visscher, A. P. Cox and J. A. R. van Veen, *Electrochim. Acta*, 1995, **40**, 1537–1543.

